J. Phys.: Condens. Matter **22** (2010) 145302 (6pp) doi:10.1088/0953-8984/22/14/145302

The formation of wrinkles in single-layer graphene sheets under nanoindentation

A J Gil[1], S Adhikari[1], F Scarpa[2] and J Bonet[1]

[1] School of Engineering, Swansea University, Singleton Park, Swansea SA2 8PP, UK
[2] Advanced Composites Centre for Innovation and Science, University of Bristol, Bristol BS8 1TR, UK

E-mail: A.J.Gil@Swansea.ac.uk, S.Adhikari@swansea.ac.uk, f.scarpa@bris.ac.uk and J.Bonet@swansea.ac.uk

Received 7 January 2010, in final form 1 March 2010
Published 23 March 2010
Online at stacks.iop.org/JPhysCM/22/145302

Abstract
We investigate the formation of wrinkles and bulging in single-layer graphene sheets using an equivalent atomistic continuum nonlinear hyperelastic theory for nanoindentation and nanopressurization. We show that nonlinear geometrical effects play a key role in the development of wrinkles. Without abandoning the classical tension field membrane theory, we develop an enhanced model based upon the minimization of a relaxed energy functional in conjunction with nonlinear finite hyperelasticity. Formation of wrinkles are observed in rectangular graphene sheets due to the combination of induced membrane tension and edge effects under external pressure.

(Some figures in this article are in colour only in the electronic version)

1. Introduction

Spontaneous ripples and wrinkling have been identified for the first time by Meyer *et al* [1] on free-standing graphene sheets through a vacuum between metal struts. A taxing problem is the explanation of the origin of the wrinkles, as well as a phenomenological description of the mechanics involved in the generation of ripples. Edge stress-induced warping and instability has been investigated using both an analytical [2] and first-principles study [3]. The existence of stress in suspended graphene sheets has also been confirmed by other authors [4]. More recently the folding of graphene sheets has been discussed in [5]. Fasolino *et al* [6] have assumed possible thermal fluctuations as the cause of the ripples. This hypothesis has been challenged by Thompson-Flagg *et al* [7], who proposed a deformation mechanism induced by random distributions of OH groups over the free-standing graphene sheets. MD simulations using the MEAM potential [8] show that the functional groups induce localized lengthening of the C–C bonds, with static buckling similar to the ones in leaves. When 20% of the graphene sheet surface is covered by adsorbates, the ripples simulated by the MD approach are consistent with the experimental results (2–20 Å height over 200 Å of length). The origin of wrinkles and ripples due to the presence of OH groups is interesting, in view of the role that these adsorbates play in the generation of graphene [9, 10]. It is, however, important to distinguish between two separate issues: the intrinsic corrugation of graphene and wrinkling brought on by a loading of the graphene sheet. The former represents a corrugation of the whole sample, while the latter is localized in finite regions at the sample edges (the Saint Venant effect). In this paper we study the possibility of wrinkling of a graphene sheet without considering the effect of the OH groups, which may be considered as impurities. We assume that the graphene sheet is without any ripples before the application of pressure and nanoindentation.

Graphene sheets have been proposed as platforms for mass and/or gas sensors due to the sensitivity to change in bending/membrane stiffness under thermal and mechanical (static and dynamic) loading [11–18]. While most of the models related to out-of-plane deformation of graphene sheets available in the open literature are based on combinations of flexural and membrane stiffness [19–23], membrane-dominated deformations are the ones that provide the phenomena of wrinkles and ripples in continuum-like structural plates [24–27]. In this work, we show that wrinkling phenomena on graphene sheets can be described using a hyperelastic representation of the graphene sheets subjected to external out-of-plane mechanical loading. The model is validated against both existing experimental and numerical

results from atomistic and molecular mechanics simulations related to point force loading, and used to predict bulging and ripples in rectangular graphene sheets subjected to external pressure, which could represent external mass or functional group distributions.

2. Mathematical model and analysis

Experimental data on the out-of-plane properties of graphene have been made available on multilayer [19] and single-layer sheets (SLGS) loaded with atomic force microscope (AFM) tips [28]. Specific out-of-plane SLGS simulations have been carried out using a meshless approach [29], continuum mechanics representations based on MD force models [22, 30], while the flexural behaviour of SLGS has been modelled in resonance mode using continuum- and truss-like structural assemblies [23, 31–39]. Due to the intrinsic nature of membrane structures (such as a graphene sheet), which can withstand loading normal to the local tangent plane by means of in-plane tension stresses, nonlinear geometric effects cannot be disregarded in the formulation. Hence, nonlinear continuum mechanics principles [24] are vital instruments in order to capture the nonlinearity of the problem. Let $\{\boldsymbol{N}_\alpha\}^{\alpha=1,2,3}$ be the unit orthogonal triad which defines the principal directions corresponding to the right Cauchy–Green deformation tensor $\boldsymbol{C}$. Following the deformation process defined by the gradient tensor $\boldsymbol{F}$, the triad transforms into the unit orthogonal triad $\{\boldsymbol{n}_\alpha\}^{\alpha=1,2,3}$ corresponding to the principal directions of the left Cauchy–Green deformation tensor $\boldsymbol{b}$ according to $\lambda_\alpha \boldsymbol{n}_\alpha = \boldsymbol{F}\boldsymbol{N}_\alpha$, where λ_α symbolizes the principal stretches. The vector components of both triads have been ordered such that the third one is always aligned along the normal to the local tangent plane of the membrane. Thus, the Cauchy stress tensor $\boldsymbol{\sigma}$ admits a spectral decomposition in terms of its eigenvalues $\sigma_{\alpha\alpha}$ as

$$\boldsymbol{\sigma} = \sum_{\alpha=1}^{2} \sigma_{\alpha\alpha} \boldsymbol{n}_\alpha \otimes \boldsymbol{n}_\alpha; \qquad \sigma_{\alpha\alpha} = \frac{\lambda_\alpha}{J}\frac{\partial \psi}{\partial \lambda_\alpha}; \qquad J = \lambda_1\lambda_2\lambda_3 \tag{1}$$

where ψ stands for the Helmholtz free energy functional for a plane stress Saint-Venant–Kirchhoff hyperelastic material and J represents the Jacobian of the deformation. The evaluation of the terms $\sigma_{\alpha\alpha}$ in equation (1) can be straightforwardly carried out as the in-plane energy functional ψ is formulated as

$$\psi(\lambda_1, \lambda_2) = \frac{\bar{\lambda}}{4}(\lambda_1^2 + \lambda_2^2 - 2) + \frac{\mu}{4}(\lambda_1^2 - 1)(\lambda_2^2 - 1) \tag{2}$$

where $\bar{\lambda} = \frac{2\lambda\mu}{\lambda+2\mu}$ and λ and μ symbolize the well-known Lamè coefficients. Following [24], the symmetrized constitutive fourth-order tensor $\boldsymbol{c}$ can be formulated in its spectral decomposition as

$$\boldsymbol{c} = \sum_{\alpha,\beta=1}^{2} \frac{1}{J}\frac{\partial^2\psi}{\partial \ln\lambda_\alpha \partial \ln\lambda_\beta}\boldsymbol{t}_1^{\alpha\beta} - \sum_{\alpha=1}^{2}\frac{2\lambda_\alpha}{J}\frac{\partial\psi}{\partial\lambda_\alpha}\boldsymbol{t}_2^{\alpha\beta} + \sum_{\alpha\neq\beta=1}^{2}\left[\frac{1}{\lambda_\alpha^2 - \lambda_\beta^2}\left(\frac{\lambda_\alpha\lambda_\beta^2}{2J}\frac{\partial\psi}{\partial\lambda_\alpha} - \frac{\lambda_\alpha^2\lambda_\beta}{2J}\frac{\partial\psi}{\partial\lambda_\beta}\right)\right]\boldsymbol{t}_3^{\alpha\beta} \tag{3}$$

where

$$\boldsymbol{t}_1^{\alpha\beta} = \boldsymbol{n}_\alpha \otimes \boldsymbol{n}_\alpha \otimes \boldsymbol{n}_\beta \otimes \boldsymbol{n}_\beta$$

$$\boldsymbol{t}_2^{\alpha\beta} = \boldsymbol{n}_\alpha \otimes \boldsymbol{n}_\alpha \otimes \boldsymbol{n}_\alpha \otimes \boldsymbol{n}_\alpha$$

$$\boldsymbol{t}_3^{\alpha\beta} = (\boldsymbol{n}_\alpha \otimes \boldsymbol{n}_\beta + \boldsymbol{n}_\beta \otimes \boldsymbol{n}_\alpha) \otimes (\boldsymbol{n}_\alpha \otimes \boldsymbol{n}_\beta + \boldsymbol{n}_\beta \otimes \boldsymbol{n}_\alpha).$$

In equation (3), when $\lambda_1 = \lambda_2$ the term within the brackets on the right-hand side must be replaced by

$$\frac{1}{4J}\left[\frac{\partial^2\psi}{\partial \ln\lambda_\beta \partial \ln\lambda_\beta} - \frac{\partial^2\psi}{\partial \ln\lambda_\alpha \partial \ln\lambda_\beta}\right]. \tag{4}$$

If the prestressing effect is considered prior to the load on graphene sheets, it was shown [40, 41] that the total deformation path of a prestressed membrane structure can be decomposed into two successive loading stages. In the first stage, the membrane is prestressed, deforming from an initial unstressed configuration Ω_0 to an intermediate prestressed configuration Ω_p. In the second stage, in-service loads are applied, deforming the prestressed membrane to its final configuration Ω. As a result, a modified Saint-Venant–Kirchhoff hyperelastic energy functional ψ^{mod} is proposed [40, 41] in order to account for prestressing effects:

$$\psi^{\text{mod}}(\boldsymbol{E}) = \psi(\boldsymbol{E}) + \psi^{\text{p}}(\boldsymbol{E}); \qquad \psi^{\text{p}}(\boldsymbol{E}) = \boldsymbol{\sigma}^{\text{p}}{:}\boldsymbol{E}. \tag{5}$$

Here $\boldsymbol{\sigma}^{\text{p}}$ represents the in-plane prestressing stress tensor. The in-plane Green Lagrange strain tensor $\boldsymbol{E}$ gathers the strain as a result of the deformation during the second loading stage. Moreover, in [42] it is demonstrated that the functional ψ^{mod} is convex as established in [43], thus well defined for minimization purposes. It is interesting to notice that tensors $\boldsymbol{\sigma}^{\text{p}}$ and $\boldsymbol{E}$ do not commute in general, except when $\boldsymbol{\sigma}^{\text{p}}$ is isotropic. Therefore, the final Cauchy stress tensor displayed in formula (1) must be modified to include the prestressing effect. Thus, the functional ψ is replaced by ψ^{mod} in the second of the formulae in (1). The constitutive fourth-order tensor does not need any modification.

3. Wrinkling considerations

Without abandoning the membrane theory, we develop an enhanced model with the purpose of avoiding the spurious compressive stresses generated by the classical tension field theory. In this approach, following [42–44], the ordinary energy functional is replaced by a relaxed energy functional. The in-plane principal stresses are denoted by σ_{11} and σ_{22} and, after arranging in such a way that $\sigma_{11} \geqslant \sigma_{22}$, the three states of a wrinkled membrane can be summarized as: *taut state* ($\sigma_{11} > 0, \sigma_{22} > 0$), *wrinkled state* ($\sigma_{11} > 0, \sigma_{22} = 0$) and *slack state* ($\sigma_{11} = 0, \sigma_{22} = 0$). In this way, the onset of wrinkling can be characterized when the smallest of the principal stresses σ_{22} reaches a null value. When this consideration is taken into account, a kinematic constraint can be established between both in-plane principal stretches λ_1 and λ_2, as

$$\frac{\lambda_2}{J}\frac{\partial\psi^{\text{mod}}}{\partial\lambda_2} = 0. \tag{6}$$

Thus, yielding

$$\lambda_2 = f(\lambda_1) := \left[1 + \nu(1-\lambda_1^2) + \frac{2(\nu^2-1)}{E}\left(\boldsymbol{n}_2^{\mathrm{T}}\boldsymbol{\sigma}^{\mathrm{p}}\boldsymbol{n}_2\right)\right]^{1/2} \tag{7}$$

where in the above formula $\nu = \frac{\lambda}{2(\lambda+\mu)}$ is the classical Poisson ratio and $E = \frac{\mu(2\mu+3\lambda)}{\lambda+\mu}$ represents Young's modulus. This constraint $f(\lambda_1)$ can be substituted into the in-plane energy functional ψ^{mod} defined in equation (5) to obtain a modified energy functional $\psi^{\mathrm{mod}'}$:

$$\psi^{\mathrm{mod}'}(\boldsymbol{E}) = \psi'(\boldsymbol{E}) + \psi^{\mathrm{p}'}(\boldsymbol{E}) \tag{8}$$

in which

$$\psi'(\boldsymbol{E}) = \frac{E}{8}(\lambda_1^2-1)^2 \tag{9}$$

and

$$\psi^{\mathrm{p}'}(\boldsymbol{E}) = (\boldsymbol{n}_1^{\mathrm{T}}\boldsymbol{\sigma}^{\mathrm{p}}\boldsymbol{n}_1)\tfrac{1}{2}(\lambda_1^2-1) + (\boldsymbol{n}_2^{\mathrm{T}}\boldsymbol{\sigma}^{\mathrm{p}}\boldsymbol{n}_2)\tfrac{1}{2}(f(\lambda_1)^2-1). \tag{10}$$

Thus, the modified Cauchy stress tensor $\boldsymbol{\sigma}'$ takes the form

$$\boldsymbol{\sigma}' = \sigma_{11}\boldsymbol{n}_1 \otimes \boldsymbol{n}_1; \qquad \sigma_{11} = \frac{\lambda_1}{J}\frac{\partial \psi^{\mathrm{mod}'}}{\partial \lambda_1}. \tag{11}$$

After applying some straightforward algebra, it yields

$$\sigma_{11} = \frac{\lambda_1^2}{J}\left[\frac{E}{2}(\lambda_1^2-1) + \left(\boldsymbol{n}_1^{\mathrm{T}}\boldsymbol{\sigma}^{\mathrm{p}}\boldsymbol{n}_1\right) + \nu\left(\boldsymbol{n}_2^{\mathrm{T}}\boldsymbol{\sigma}^{\mathrm{p}}\boldsymbol{n}_2\right)\right]. \tag{12}$$

Analogously, the modified constitutive fourth-order tensor can be deduced from equation (3) after replacing ψ with ψ' where required, resulting in

$$\boldsymbol{c}' = \frac{E\lambda_1^4}{J}\boldsymbol{t}_1 + \frac{E\lambda_1^2\lambda_2^2}{4J}\frac{(\lambda_1^2-1)}{(\lambda_1^2-\lambda_2^2)}\boldsymbol{t}_2 \tag{13}$$

where

$$\boldsymbol{t}_1 = \boldsymbol{n}_1 \otimes \boldsymbol{n}_1 \otimes \boldsymbol{n}_1 \otimes \boldsymbol{n}_1$$

$$\boldsymbol{t}_2 = (\boldsymbol{n}_1 \otimes \boldsymbol{n}_2 + \boldsymbol{n}_2 \otimes \boldsymbol{n}_1) \otimes (\boldsymbol{n}_1 \otimes \boldsymbol{n}_2 + \boldsymbol{n}_2 \otimes \boldsymbol{n}_1).$$

Finally, the condition that must be fulfilled for wrinkling to occur in both principal directions is that the principal Cauchy stresses σ_{11} and σ_{22} must be zero simultaneously:

$$\frac{\lambda_1}{J}\frac{\partial \psi^{\mathrm{mod}}}{\partial \lambda_1} = 0. \tag{14}$$

Thus, resulting in

$$\lambda_1 = g := \left[1 + \frac{2(\nu-1)}{E}\left(\boldsymbol{n}_2^{\mathrm{T}}\boldsymbol{\sigma}^{\mathrm{p}}\boldsymbol{n}_2\right)\right]^{1/2}. \tag{15}$$

It is important to emphasize that, on the one hand, the methodology outlined here takes into consideration large strains in a manner consistent with classical continuum mechanics, and on the other hand, is derived according to standard tension field theory, where the mechanical membrane response is predominant over the bending response. Indeed, in [28] it is reported that, even at maximum curvature, the energy from bending in the graphene membrane is three orders of magnitude smaller than the energy from in-plane strain. It is also observed that this methodology allows the consideration of prestress effects as well as more sophisticated constitutive models (if needed) through a suitable modification of Helmholtz's free energy functional. Finally, this formulation enables the study of wrinkling patterns through the visualization of the null principal Cauchy stress regions.

4. Results and discussion

The first example discussed in this section is a circular flat graphene sheet, with its boundary fully clamped, which is subjected to a transverse point load applied at its centre. Isotropic elastic mechanical properties are considered to model the constitutive behaviour of the graphene sheet.

As is well known, there is no closed-form analytical solution that accounts for both finite (i.e. large) deformation as well as possible pretension in a material. However, in [28], the following force–displacement relationship is considered:

$$F = \sigma_0 h\pi\delta + Eh(aq^3)\left(\frac{\delta}{a}\right)^3 \tag{16}$$

where F is the applied force, δ is the deflection at the centre point, a is the radius of the circular membrane, σ_0 is a possible in-plane pretension stress of the graphene membrane, $q = 1/(1.05 - 0.15\nu - 0.16\nu^2)$ is a dimensionless parameter expressed in terms of the Poisson ratio ν, E is the so-called Young's modulus and h is the thickness of the graphene membrane. This simple approximated formula can be regarded as valid in the case of axisymmetric membranes subjected to initial in-plane prestress, a centrally located transverse point load and fulfilling the assumption of moderate displacements, the latter as highly nonlinear strain terms appearing under very large displacements are neglected in its derivation (von Karman compatibility equations). In [28], an extensive series of experimental results were fitted to the above formula (16) under the free parameters E and σ_0. In the results presented in figure 1, two alternative radii are considered, namely $a = 0.5$ and 0.75 μm for the same thickness $h = 0.335$ nm. Following [28], $\nu = 0.165$ and average values of $Eh = 342$ N nm^{-1} and $\sigma_0 h = 0.34$ N nm^{-1} are employed. Uncertainty analyses for the various measured variables during the experiments are also presented in [28]. In the present study, a finite element implementation of the algorithm described in section 3 is employed in order to compare its validity with respect to experimental results. For computational purposes, a sufficiently refined mesh is used comprised of 1936 three-noded isoparametric linear finite elements to ensure mesh convergence of the numerical solution (only one quarter of the membrane is analysed under suitable boundary conditions). Numerical and experimental results are extremely similar, especially for moderate values of displacement (up to 1500 nN of force). It can be noted that, in the large strain regime, the experimental and numerical results start to differ slightly. This indicates that the inclusion of a more sophisticated hyperelastic

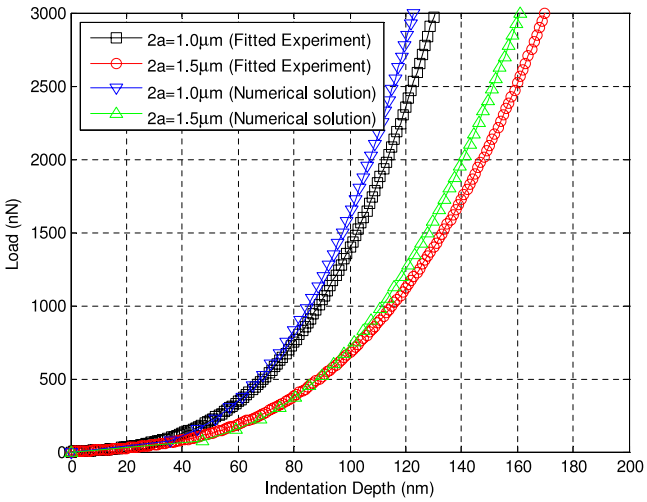

Figure 1. Force (nN) versus indentation deflection (nm) computation for a single-layer graphene sheet with circular geometry under central point load. The proposed approach is compared with experimental results for two different radii. Numerical and experimental results are close for moderate values of displacements: however, they start to differ for higher values of displacements.

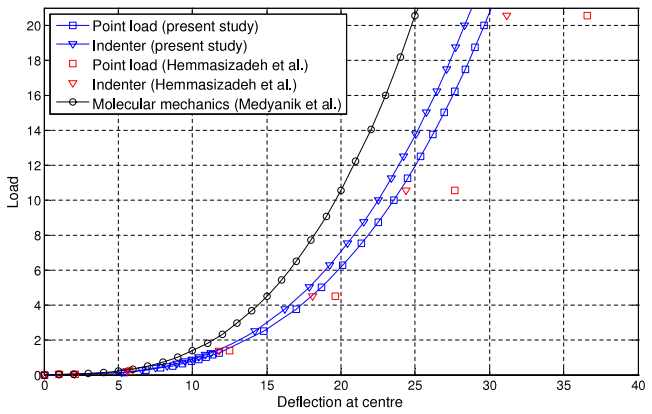

Figure 2. Force (eV Å^{-1}) versus indentation deflection (Å) computation for a single-layer graphene sheet with circular geometry. The proposed approach and few existing approaches are compared with molecular mechanics simulation. All the methods show a softening effect compared to the molecular mechanics simulation results. The approach proposed here is the closest to the molecular mechanics simulation for the large deflection cases.

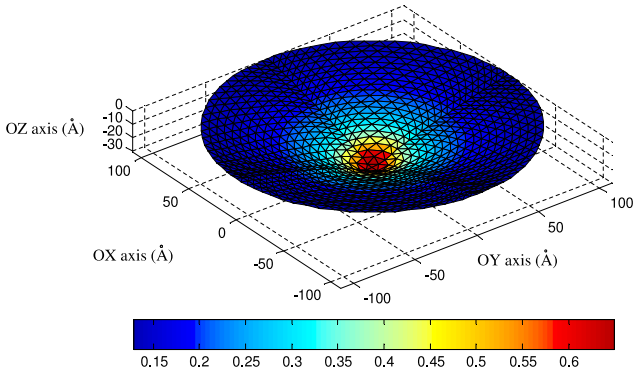

Figure 3. Maximum Cauchy principal stress (eV Å^{-3}) of a clamped circular graphene sheet under a point load applied at the centre (FEM mesh: 1936 three-noded isoparametric linear finite elements). The colour bar shows intensity of stress in the centrally loaded graphene sheet. The maximum stress occurs below the application of the load.

constitutive model (i.e. neo-Hookean or Mooney–Rivlin) [24] could help to characterize more accurately the mechanical behaviour of the graphene sheet.

A second example is studied, where a circular flat graphene sheet of radius 110 Å and Poisson's ratio $\nu = 0.19$ is subjected to a point load applied at its centre, ensuring that its boundary is fully clamped. Two loading scenarios are taken into consideration: in the first, a point load is applied at the centre of the circular graphene sheet whereas in the second the same load is distributed across a circular area of radius 10 Å, which is the indenter loading scenario. Young's modulus E and the thickness h for the numerical experiment are taken from Hemmasizadeh *et al* [30]. This problem is analysed in [30] considering small strains and bending deformation. A cubic polynomial relating the applied load and deflection at the centre of the graphene membrane is best fitted to the results provided by molecular mechanics simulation in Medyanik *et al* [45]. Consequently, the values of $E = 5.864$ eV Å^{-3} and $h = 1.37$ Å taken from [30] are here adopted for subsequent numerical simulations. Figure 2 shows the results according to various methods. The value of the thickness h varies in the open literature, whether first-or second-generation Tersoff–Brenner potentials [46], or equivalent atomistic—continuum models for SLGS loaded in-plane [38]. A COMPASS force field applied to continuum plate von Karman equations with membrane field has provided a value of $h = 0.52$ Å for a point load circular SLGS of 80 Å [47]. Hemmasizadeh *et al* [30] compare the molecular dynamics simulation with their computational finite element analysis by using a four-node doubly curved shell (accounting for bending stiffness) elements. In the present study, a pure membrane formulation with a wrinkling algorithm based upon a modified energy functional is used for the same example in order to demonstrate the accuracy of the method. For both loading cases, the formulation presented shows accurate results in comparison with the molecular mechanics simulation, despite not including any bending stiffness. For computational purposes, a sufficiently refined mesh is used comprised of 1936 three-noded isoparametric linear finite elements to ensure mesh convergence of the numerical solution. The maximum Cauchy principal stress contour plot is shown in figure 3. A horizontal colour bar at the bottom of the figure displays the range of values for the maximum Cauchy principal stress, ranging from 0.125 eV Å^{-3} near the clamped boundary up to 0.65 eV Å^{-3} located near the indentation load, highlighting, as expected, the Saint-Venant effect.

With the purpose of investigating the behaviour of the graphene sheet undergoing wrinkling, a different example is analysed. A square flat graphene membrane of side 220 Å is subjected to an internal pressure load $p = 5.165\,29 \times 10^{-4}$ eV Å^{-3}, acting normal to the local tangent plane of the membrane, which introduces an extra nonlinearity within the algorithm which requires suitable consideration [48]. The boundary of the squared membrane is free to move but forced

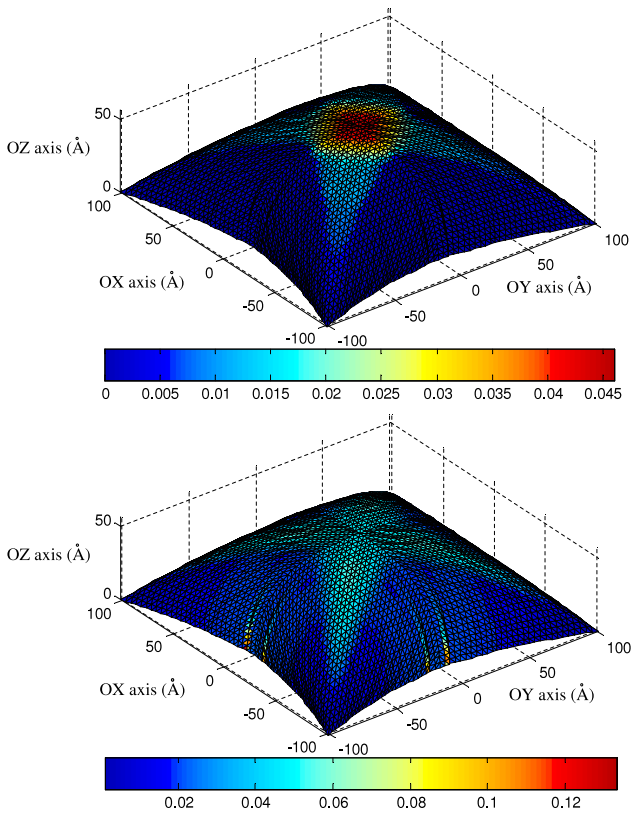

Figure 4. The bulging of graphene sheets under pressure: (top) minimum Cauchy principal stress (eV Å^{-3}), (bottom) maximum Cauchy principal stress (eV Å^{-3}), FEM mesh: 7200 three-noded isoparametric linear finite elements. Wrinkling can be observed on every side of the SLGS.

to remain within its original plane. The material properties and the thickness of the specimen are identical to those of the previous example. Figure 4 displays contour plots for the minimum Cauchy principal stress (top) and the maximum Cauchy principal stress (bottom). Colour bars at the bottom of every figure show the range of values for the minimum (top) and the maximum (bottom) Cauchy principal stress. As can be observed, wrinkles start to develop in every side of the SLGS under consideration, where the maximum values for the maximum Cauchy principal stress are attained, as well as null values of the minimum Cauchy stress. Moreover, it can be noticed that no negative values for the minimum Cauchy principal stress are achieved, as the range of values expands from 0 to 0.045 eV Å^{-3}, demonstrating the use of the wrinkling algorithm employed. For computational purposes, a sufficiently refined mesh is used comprised of 7200 three-noded isoparametric linear finite elements to ensure mesh convergence of the numerical solution. This methodology enables the visualization of wrinkling patterns by observing areas of null minimum principal Cauchy stress, without the need to resort to computationally expensive algorithms with shell capability. In addition, as wrinkling patterns appear only in localized finite regions (i.e. the Saint-Venant effect) of the graphene sheet where extreme curvature values are reached, this tension field algorithm remains extremely valuable and enables the extraction of information related to overall force–displacement relationship or mechanical properties such as Young's modulus and pretension stress.

5. Conclusion

In this paper we considered wrinkling and bending of single-layer graphene sheets under nanoindentation and nanopressurization. Both rectangular and circular graphene sheets are considered. The proposed approach employs pure tension field membrane theory, neglecting bending effects, where minimization of a relaxed energy functional is carried out within the context of large-deformation finite strains in order to account for geometric nonlinear effects. One of the main novelties is the consistent and rigorous treatment of nonlinearity and prestress, crucial for the out-of-plane deformation of graphene sheets. The formation of wrinkling patterns can be observed through the visualization of the null principal stress regions. The presented methodology shows excellent agreement with published numerical and experimental results on out-of-plane deflection of graphene sheets due to nanoindentation. We also studied the bulging of rectangular graphene sheets under pressure where the formation of wrinkles is observed along the edges.

Acknowledgment

SA gratefully acknowledges the support of The Leverhulme Trust for the award of the Philip Leverhulme Prize.

References

[1] Meyer J C, Geim A K, Katsnelson M I, Novoselov K S, Booth T J and Roth S 2007 The structure of suspended graphene sheets *Nature* **446** 60–3
[2] Shenoy V B, Reddy C D, Ramasubramaniam A and Zhang Y 2008 Edge-stress-induced warping of graphene sheets and nanoribbons *Phys. Rev. Lett.* **101** 245501
[3] Huang B, Liu M, Su N, Wu J, Duan W, Gu B L and Liu F 2009 Quantum manifestations of graphene edge stress and edge instability: a first-principles study *Phys. Rev. Lett.* **102** 166404
[4] Garcia-Sanchez D, van der Zande A M, Paulo A S, Lassagne B, McEuen P L and Bachtold A 2008 Imaging mechanical vibrations in suspended graphene sheets *Nano Lett.* **8** 1399–403
[5] Cranford S, Sen D and Buehler M J 2009 Meso-origami: folding multilayer graphene sheets *Appl. Phys. Lett.* **95** 123121
[6] Fasolino A, Los J H and Katsnelson M I 2007 Intrinsic ripples in graphene *Nat. Mater.* **6** 858–61
[7] Thompson-Flagg R C, Moura M J B and Marder M 2009 Rippling of graphene *Eur. Phys. Lett.* **85** 46002
[8] Baskes M, Angelo J and Bisson C 1994 Atomistic calculations of composite interfaces *iUTAM Symp. on Computational Mechanics of Materials (Providence, RI, June 1993)*; *Modell. Simul. Mater. Sci. Eng.* **2** 505–18
[9] Elias D C, Nair R R, Mohiuddin T M G, Morozov S V, Blake P, Halsall M P, Ferrari A C, Boukhvalov D W, Katsnelson M I, Geim A K and Novoselov K S 2009 Control of graphene's properties by reversible hydrogenation: evidence for graphane *Science* **323** 610–3
[10] Sofo J O, Chaudhari A S and Barber G D 2007 Graphane: a two-dimensional hydrocarbon *Phys. Rev.* B **75** 153401

[11] Jensen K, Kim K and Zettl A 2008 An atomic-resolution nanomechanical mass sensor *Nat. Nanotechnol.* **3** 533–7
[12] Arsat R, Breedon M, Shafiei M, Spizziri P G, Gilje S, Kaner R B, Kalantar-Zadeh K and Wlodarski W 2009 Graphene-like nano-sheets for surface acoustic wave gas sensor applications *Chem. Phys. Lett.* **467** 344–7
[13] Sakhaee-Pour A, Ahmadian M T and Vafai A 2008 Potential application of single-layered graphene sheet as strain sensor *Solid State Commun.* **147** 336–40
[14] Rangel N L and Seminario J A 2008 Graphene terahertz generators for molecular circuits and sensors *J. Phys. Chem.* A **112** 13699–705
[15] Mohanty N and Berry V 2008 Graphene-based single-bacterium resolution biodevice and DNA transistor: interfacing graphene derivatives with nanoscale and microscale biocomponents *Nano Lett.* **8** 4469–76
[16] Moradian R, Mohammadi Y and Ghobadi N 2008 Investigation of gas sensing properties of armchair graphene nanoribbons *J. Phys.: Condens. Matter* **20** 425211
[17] Sakhaee-Pour A, Ahmadian M T and Vafai A 2008 Applications of single-layered graphene sheets as mass sensors and atomistic dust detectors *Solid State Commun.* **145** 168–72
[18] Hadlington S 2007 Graphene sensor achieves ultimate sensitivity *Chem. World* **4** 29
[19] Frank I W, Tanenbaum D M, van der Zande A M and McEuen P L 2007 Mechanical properties of suspended graphene sheets *J. Vac. Sci. Technol.* B **25** 2558–61
[20] Lee C, Wei X, Kysar J W and Hone J 2008 Measurement of the elastic properties and intrinsic strength of monolayer graphene *Science* **321** 385–8
[21] Hemmasizadeh A, Mahzoon M and Hadi E 2008 A method for developing the equivalent continuum model of a single layer graphene sheet *Thin Solids Films* **416** 7636
[22] Duan W H and Wang C M 2009 Nonlinear bending and stretching of a circular graphene sheet under a central point load *Nanotechnology* **20** 075702
[23] Sakhaee-Pour A, Ahmadian M T and Naghdabadi R 2008 Vibrational analysis of single-layered graphene sheets *Nanotechnology* **19** 085702
[24] Bonet J and Wood R D 2008 *Nonlinear Continuum Mechanics for Finite Element Analysis* 2nd edn (Cambridge: Cambridge University Press)
[25] Efimenko K, Rackaitis M, Manias E, Vaziri A, Mahadevan L and Genzer J 2005 Nested self-similar wrinkling patterns in skins *Nat. Mater.* **4** 293–7
[26] Cerda E and Mahadevan L 2003 Geometry and physics of wrinkling *Phys. Rev. Lett.* **90** 074302
[27] Cerda E, Ravi-Chandar K and Mahadevan L 2002 Thin films—wrinkling of an elastic sheet under tension *Nature* **419** 579–80
[28] Lee C, Wei X, Kysar J W and Hone J 2008 Measurement of the elastic properties and intrinsic strength of monolayer graphene *Science* **321** 385–8
[29] Medyanik S N, Karpov E G and Liu W K 2006 Domain reduction method for atomistic simulations *J. Comput. Phys.* **218** 836–59
[30] Hemmasizadeh A, Mahzoon M, Hadi E and Khandan R 2008 A method for developing the equivalent continuum model of a single layer graphene sheet *Thin Solids Films* **416** 7636
[31] Gupta S S and Batra R C 2010 Elastic properties and frequencies of free vibrations of single-layer graphene sheets *J. Comput. Theor. Nanosci.* **31** at press
[32] Batra R C and Sears A 2007 Continuum models of multi-walled carbon nanotubes *Int. J. Solids Struct.* **44** 7577–96
[33] Sakhaee-Pour A 2009 Elastic buckling of single-layered graphene sheet *Comput. Mater. Sci.* **45** 266–70
[34] Sakhaee-Pour A 2009 Elastic properties of single-layered graphene sheet *Solid State Commun.* **149** 91–5
[35] Odegard G M, Gates T S, Nicholson L M and Wise K E 2002 Equivalent-continuum modeling of nano-structured materials *Composit. Sci. Technol.* **62** 1869–80
[36] Tserpes K I and Papanikos P 2005 Finite element modelling of single-walled carbon nanotubes *Composite* B **36** 468
[37] Scarpa F and Adhikari S 2008 A mechanical equivalence for the Poisson's ratio and thickness of C–C bonds in single wall carbon nanotubes *J. Phys. D: Appl. Phys.* **41** 085306
[38] Scarpa F, Adhikari S and Phani A S 2009 Effective elastic mechanical properties of single layer graphene sheets *Nanotechnology* **20** 065709
[39] Scarpa F, Adhikari S and Wang C Y 2009 Mechanical properties of non-reconstructed defective single-wall carbon nanotubes *J. Phys. D: Appl. Phys.* **42** 142002
[40] Gil A J 2006 Structural analysis of prestressed Saint Venant–Kirchhoff hyperelastic membranes subjected to moderate strains *Comput. Struct.* **84** 1012
[41] Gil A J and Bonet J 2006 Finite element analysis of prestressed structural membranes *Finite Elem. Anal. Des.* **42** 683
[42] Gil A J and Bonet J 2007 Finite element analysis of partly wrinkled reinforced prestressed membranes *Comput. Mech.* **40** 595
[43] Pipkin A C 1986 The relaxed energy density for isotropic elastic membranes *IMA J. Appl. Math.* **36** 85
[44] Steigmann D J and Pipkin A C 1989 Wrinkling of pressurized membranes *J. Appl. Mech.* **56** 624
[45] Medyanik S N, Karpov E G and Liu W K 2006 Domain reduction method for atomistic simulations *J. Comput. Phys.* **218** 836
[46] Huang Y, Wu J and Hwang K C 2006 Thickness of graphene and single-wall carbon nanotubes *Phys. Rev.* B **74** 245413
[47] Duan W H and Wang C M 2009 Nonlinear bending and stretching of a circular graphene sheet under a central point load *Nanotechnology* **20** 075702
[48] Simo J C, Taylor R L and Wriggers P 1991 A note on finite element implementation of pressure boundary loading *Commun. Appl. Numer. Methods* **7** 513